Energy & Environmental Science

COMMUNICATION

View Article Online
View Journal | View Issue

Cite this: *Energy Environ. Sci.*, 2016, **9**, 2011

Received 9th March 2016,
Accepted 20th April 2016

DOI: 10.1039/c6ee00728g

www.rsc.org/ees

The origin of low thermal conductivity in $Sn_{1-x}Sb_xTe$: phonon scattering *via* layered intergrowth nanostructures†

Ananya Banik,[a] Badri Vishal,[bc] Suresh Perumal,[a] Ranjan Datta[bc] and Kanishka Biswas*[a]

Inorganic solids with low thermal conductivity are of great interest for thermoelectric applications. The formation of synthetic nanostructures by matrix encapsulation is one of the important strategies for thermal conductivity reduction through phonon scattering. Here, we report the reduction of lattice thermal conductivity near the theoretical minimum limit, κ_{min}, in SnTe *via* spontaneous formation of nanodomains of the Sb-rich layered intergrowth $Sn_mSb_{2n}Te_{3n+m}$ compounds, which are natural heterostructures. High-resolution transmission electron microscopy of $Sn_{1-x}Sb_xTe$ samples reveals the formation of endotaxial Sb rich nanoprecipitates (2–10 nm) along with super-structured intergrowth nanodomains (10–30 nm), which are the key features responsible for the significant reduction of lattice thermal conductivity in SnTe. This mechanism suggests a new avenue for the nanoscale engineering in SnTe to achieve low lattice thermal conductivities. Moreover, the presence of Sb improves the electronic transport properties by aliovalent cation doping which optimizes the hole concentration in SnTe. As a result, an enhanced thermoelectric figure of merit, *zT*, of ~1 has been achieved for the composition of $Sn_{0.85}Sb_{0.15}Te$ at 800 K. The high *zT* sample exhibits the Vickers microhardness value of ~136 H_V which is double that of pristine SnTe and is significantly higher than those of the present state-of-the-art thermoelectric materials.

Broader context

Tin telluride (SnTe), a homologue of lead telluride (PbTe), has recently attracted enormous attention for the thermoelectric power generation in the mid-temperature range. However, the thermoelectric properties of SnTe have been mostly improved *via* electronic structure engineering either by creating resonant states in the electronic band or by valence band convergence. Pristine SnTe exhibits a lattice thermal conductivity (κ_{lat}) of ~2.88 W m^{-1} K^{-1} at room temperature, while the theoretical limit for the minimum lattice thermal conductivity (κ_{min}) of SnTe is ~0.5 W m^{-1} K^{-1}. This hints at the presence of enormous room to improve the *zT* through κ_{lat} reduction in SnTe. Although κ_{lat} has been moderately reduced *via* the introduction of second phase nanoprecipitates or alloy formation, very few reports exist which could successfully reduce the κ_{lat} value of SnTe near its theoretical minimum value. Here, we report the reduction of κ_{lat} to ~0.67 W m^{-1} K^{-1} at room temperature, which is close to its theoretical minimum limit, κ_{min}, *via* the spontaneous formation of nanodomains of the Sb-rich layered intergrowth $Sn_mSb_{2n}Te_{3n+m}$ compounds in the SnTe matrix. High-resolution transmission electron microscopy of $Sn_{1-x}Sb_xTe$ samples reveals the formation of endotaxial Sb rich nanoprecipitates (2–10 nm) along with super-structured intergrowth nanodomains (10–30 nm), which are the key features for the significant reduction of κ_{lat} in SnTe. As a result, an enhanced thermoelectric figure of merit, *zT*, of ~1 has been achieved for the composition of $Sn_{0.85}Sb_{0.15}Te$ at 800 K. For the high *zT* sample, the measured Vickers microhardness (mechanical stability) value is ~136 H_V, which is 109% higher than that of pristine SnTe (~65 H_V). The present micro-hardness value is significantly higher than those of the state-of-the-art thermoelectric materials such as Bi_2Te_3, PbTe, $Pb_{1-x}Sn_xTe$, PbSe, Cu_2S, and Cu_2Se.

1. Introduction

Narrow band gap semiconductors with low lattice thermal conductivity (κ_{lat}) are important candidates for thermoelectric energy conservation. The efficiency of thermoelectric materials is mainly governed by the thermoelectric figure of merit, $zT = \sigma S^2 T/\kappa_{total}$, where σ, S, T, and κ_{total} (κ_{el}, electronic thermal

[a] *New Chemistry Unit, Jawaharlal Nehru Centre for Advanced Scientific Research (JNCASR), Jakkur P.O., Bangalore 560064, India. E-mail: kanishka@jncasr.ac.in*
[b] *Chemistry and Physics of Materials Unit, Jawaharlal Nehru Centre for Advanced Scientific Research (JNCASR), Jakkur P.O., Bangalore 560064, India*
[c] *International Centre for Materials Science, Jawaharlal Nehru Centre for Advanced Scientific Research (JNCASR), Jakkur P.O., Bangalore 560064, India*

† Electronic supplementary information (ESI) available: Temperature dependent thermal diffusivity (D) and heat capacity (C_p) of $Sn_{1-x}Sb_xTe$ (Fig. S1), heating and cooling cycles of electrical conductivity (σ), Seebeck coefficient (S), power factor (σS^2) and thermal conductivity (κ_{total}) data of $Sn_{0.88}Sb_{0.12}Te$ (Fig. S2), Vickers micro-indentation of SnTe and $Sn_{0.85}Sb_{0.15}Te$, respectively (Fig. S3); temperature dependent Lorenz number (L) of $Sn_{1-x}Sb_xTe$ (Fig. S4); comparison plot of present room-temperature lattice thermal conductivity with the KD model based lattice thermal conductivity for $Sn_{1-x}Sb_xTe$ (Fig. S5); low-magnification TEM images and HRTEM images of $Sn_{0.96}Sb_{0.04}Te$, $Sn_{0.92}Sb_{0.08}Te$ and $Sn_{0.85}Sb_{0.15}Te$ (Fig. S6), HRTEM and EDAX of the $Sn_{0.85}Sb_{0.15}Te$ sample showing the presence of Sb rich nanoprecipitates (Fig. S7) and nanoprecipitates size distribution histogram (Fig. S8). See DOI: 10.1039/c6ee00728g

conductivity + κ_{lat}, lattice thermal conductivity) are the electrical conductivity, Seebeck coefficient, temperature and total thermal conductivity, respectively.[1] The interdependence of σ, S and κ_{total} complicates the attempt for the development of high performance thermoelectric materials.[1c] The only independently tunable parameter is κ_{lat}. The reduction of the κ_{lat} value of inorganic solids has conventionally been achieved through the formation of point-defects and grain boundaries,[1,2] all-scale hierarchical nano-mesostructuring[3] and embedding endotaxial nanostructures[4] in the bulk matrix. Furthermore, intrinsically low κ_{lat}, originating in solids with lattice features such as complex crystal structures,[1c] part-crystalline part-liquid state,[5] rattling modes,[6] soft phonon modes,[7] superionic substructures with liquid-like cation disordering,[8] resonant bonding,[9] lattice anharmonicity due to lone pairs[10] and anisotropic layered crystal structure,[11] is of practical interest due to its robustness against the grain size, temperature and other structural variations.

The combination of low thermal conductivity, large thermopower and optimum electrical conductivity made PbTe the leading thermoelectric material for power generation application in the intermediate temperature range of 600–900 K.[3,4,12] However, the relative toxicity of Pb accompanied by the environmental concern limits its large scale application, which motivates the researcher to look for alternative materials for PbTe. SnTe could be a probable substituent for PbTe because of the same rock-salt crystal structure ($Fm\bar{3}m$) and similar electronic structures. However, it has a large number of p-type carriers due to the intrinsic Sn vacancy and the energy separation, ΔE, between the light hole (L point) and heavy hole (Σ point) valence bands of SnTe ($\sim$0.3–0.4 eV) is higher than that of PbTe ($\sim$0.17 eV).[13] Thus, pristine SnTe has rarely been considered as an efficient thermoelectric material.[14] However, recent studies explicitly show that SnTe has the strong potential of being a promising thermoelectric material through valence band engineering,[15] carrier concentration optimization,[15e,16] and/or all-scale hierarchical architecture.[17] Significant enhancement of the Seebeck coefficient has been achieved *via* the formation of the resonant level in the valence band of SnTe through In doping[18] and the convergence of valence band valleys by alloying of Cd, Hg, Mg or Mn in SnTe.[15a,b,d,17a,c] The coexistence of the resonant level induced by In doping and band convergence enabled by Cd doping in SnTe maximized zT up to 1.4 at 900 K.[19]

Pristine SnTe exhibits κ_{lat} of $\sim$2.88 W m^{-1} K^{-1} at room temperature, while the theoretical limit for the minimum lattice thermal conductivity (κ_{min}) of SnTe is $\sim$0.5 W m^{-1} K^{-1}.[17b] Although κ_{lat} has been moderately reduced *via* the introduction of second phase nanoprecipitates like CdS and HgTe[17a,c] or alloy formation,[15b,17b,20] only a few reports exist which could successfully reduce the κ_{lat} value of SnTe near its theoretical minimum value.[21] These approaches resulted in a κ_{lat} value close to $\sim$1 W m^{-1} K^{-1} at room temperature, which is still higher as compared to the theoretical minimum limit κ_{min} of $\sim$0.5 W m^{-1} K^{-1} for SnTe. This hints at the presence of enormous room to improve zT through κ_{lat} reduction in SnTe.

Sb plays an important role in the optimization of κ_{lat} in the PbTe based materials.[22–25] Sb in PbTe forms nanostructures *via* matrix encapsulation, which exhibits an ultralow κ_{lat} of $\sim$0.8 W m^{-1} K^{-1} at 300 K.[22] The addition of Sb in $Pb_{9.6}Sb_yTe_{10-x}Se_x$ ($y < 0.2$) is reported to form the spontaneous nano-inclusions of Sb rich phases, which resulted in low κ_{lat} and high zT.[23] Interestingly, in n-type $AgPb_mSbTe_{2+m}$ systems, compositional fluctuations at the nanoscopic level resulted in a distinct type of nanostructures, which play a key role in achieving the low κ_{lat} and high zT.[24] Moreover, the substitution of Sb in PbTe has shown a significant increase in the thermoelectric performance at higher temperatures due to the formation of Sb donor states below the conduction band of PbTe.[25] Hence, it would be interesting to study the effect of Sb on the thermoelectric properties of SnTe.

Herein, we report the realization of ultralow κ_{lat} in high quality crystalline ingots of $Sn_{1-x}Sb_xTe$. A detailed microscopic understanding of the origin of the low κ_{lat} in $Sn_{1-x}Sb_xTe$ has been discussed. Transmission electron microscopy reveals the presence of endotaxial nanoprecipitates (2–10 nm) in lower Sb containing SnTe (*e.g.* $Sn_{0.96}Sb_{0.04}Te$), whereas with higher Sb concentration (*e.g.* $Sn_{0.85}Sb_{0.15}Te$), nanodomains (10–30 nm) of layered intergrowth Sb-rich $Sn_mSb_{2n}Te_{3n+m}$ compounds spontaneously form in the SnTe matrix, which are natural heterostructures. These distinct nanostructure–matrix interfaces significantly enhance phonon scattering, which gives rise to κ_{lat} of $\sim$0.67 W m^{-1} K^{-1} in $Sn_{0.85}Sb_{0.15}Te$ near room temperature, which is indeed approaching the theoretical κ_{min} of SnTe. Additionally, aliovalent substitution of Sb^{3+} in SnTe reduces the excess hole concentration, resulting in an enhanced Seebeck coefficient. Consequently, an optimized zT of $\sim$1 has been achieved at $\sim$800 K for the $Sn_{0.85}Sb_{0.15}Te$ sample, which makes the $Sn_{1-x}Sb_xTe$ system more attractive for mid-temperature thermoelectric power generation. The high zT sample exhibits the Vickers microhardness (mechanical stability) value of $\sim$136 H_V which is double that of pristine SnTe and significantly higher than those of the present state-of-the-art thermoelectric materials.

2. Experimental section

2.1 Reagents

Tin (Alfa Aesar 99.99+ %), tellurium (Alfa Aesar 99.999+ %), and antimony (Alfa Aesar 99.999+ %) were used for the synthesis without further purification.

2.2 Synthesis

High quality crystalline ingots ($\sim$7 g) of $Sn_{1-x}Sb_xTe$ (x = 0–0.2) were synthesized by the melting reaction of appropriate ratios of high-purity starting materials of Sn, Sb and Te in a quartz tube. The tubes were sealed under vacuum (10^{-5} torr) and slowly heated to 900 °C over 12 h, then soaked for 10 h, and cooled slowly to room temperature.

2.3 Powder X-ray diffraction

Powder X-ray diffraction for all of the samples was recorded using a Cu K$_\alpha$ (λ = 1.5406 Å) radiation on a Bruker D8 diffractometer.

2.4 TEM measurements

TEM imaging was performed using an aberration corrected FEI TITAN cubed 80–300 KV transmission electron microscope operating at 300 KV. TEM samples were prepared by conventional mechanical thinning followed by Ar ion milling to perforation in order to generate a large electron transparent thin area.

2.5 Thermal conductivity

Thermal diffusivity, D, was directly measured in the range 300–873 K using a laser flash diffusivity method in a Netzsch LFA-457 (see the D *vs.* T data in Fig. S1a, ESI†). Coins with ~8 mm diameter and ~2 mm thickness were used in all of the measurements. The temperature dependent heat capacity, C_p, was derived using a standard sample (pyroceram) in LFA457, which is in good agreement with the Dulong–Petit C_p value (see Fig. S1b, ESI†). The total thermal conductivity, κ_{total}, was calculated using the formula: $\kappa_{total} = DC_p\rho$, where ρ is the density of the sample. The density of the pellets obtained was ~97% of the theoretical density.

2.6 Electrical transport

Electrical conductivity and Seebeck coefficients were measured simultaneously under a He atmosphere from room temperature to 873 K on an ULVAC-RIKO ZEM-3 instrument system. The typical sample for measurement had a parallelepiped shape with the dimension of ~2 × 2 × 8 mm^3. The longer direction coincides with the direction in which the thermal conductivity was measured. Heating and cooling cycles give repeatable electrical properties for a given sample (Fig. S2, ESI†).

2.7 Hall measurements

Carrier concentrations were determined *via* Hall coefficient measurements at room temperature using a PPMS system. A five-contact Hall-bar geometry has been used for the measurements. At 300 K, we have estimated the carrier concentration, n, from the formula: $n = 1/eR_H$, where e is the electronic charge and R_H is the Hall coefficient.

2.8 Mechanical properties

The microhardness of the samples was measured in the commercial Zwick Roell ZHU 2.5 machine using the diamond indenter on the Vickers hardness scale, where the force used was 2 N and the indent was kept for 10 s. The Vickers hardness values (kg mm^{-2}) were determined from the equation $H_V = 1.854 \times L/(2d)^2$, where L is the indentation load and $2d$ is the diagonal length of the indentation. The impressions of the indenter are shown in Fig. S3, ESI.† The uncertainty of microhardness measurements is about 5%.

3. Results and discussion

$Sn_{1-x}Sb_xTe$ (x = 0.0, 0.04, 0.08, 0.12, 0.15, 0.16 and 0.2) samples were synthesized *via* the vacuum sealed-tube melting reaction at 900 °C. Powder X-ray diffraction (PXRD) patterns of pristine and 4–8 mol% Sb containing samples could be indexed to the rock-salt SnTe structure (space group of $Fm\bar{3}m$), which shows the absence of a second phase within the detection limit of PXRD (Fig. 1a). However, for a higher Sb content ($x \geq 0.12$) in SnTe, small intensity secondary phase peaks were observed in the PXRD pattern (* mark in Fig. 1a). Second phase peaks in PXRD closely match with the PXRD pattern of the layered intergrowth Sb rich compounds belonging to the homologous series of quasibinary $(SnTe)_m(Sb_2Te_3)_n$ systems, *i.e.* $Sn_mSb_{2n}Te_{3n+m}$,[26] which are natural modulated heterostructures (see Fig. 1b). These compounds usually crystallize in anisotropic layered tetradymite Bi_2Te_2S-type structures with a large unit cell. They can also be viewed as intergrowths of SnTe-type (rocksalt) and Sb_2Te_3-type (hexagonal) phases. The lattice parameter extracted from PXRD initially decreases linearly from a = 6.294 Å to a = 6.277 Å with the increasing Sb concentration in SnTe following the Vegard's law, which indicates the solid solution nature of $Sn_{1-x}Sb_xTe$ (up to x = 0.12) samples. However, the lattice parameters of $Sn_{1-x}Sb_xTe$ compositions with $x \geq 0.12$ do not follow the Vegard's law and deviate from linearity (Fig. 1c). The presence of small intensity extra peaks in the PXRD pattern and the non-linear relationship between the lattice parameter and Sb concentration indicate the formation of $Sn_mSb_{2n}Te_{3n+m}$ intergrowth nanostructures in the SnTe matrix, which has been further confirmed *via* transmission electron microscopy analysis, which will be discussed in the following part.

The temperature dependent total thermal conductivity (κ_{total}) of $Sn_{1-x}Sb_xTe$ (x = 0.00–0.20) along with the lattice (κ_{lat}) and electronic (κ_{el}) contributions are plotted in Fig. 2. The substitution of Sb in SnTe substantially reduces the κ_{total} value from

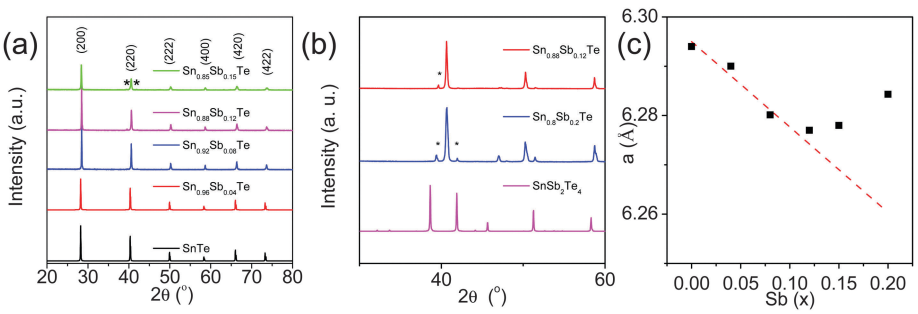

Fig. 1 (a) Powder XRD patterns of $Sn_{1-x}Sb_xTe$ (x = 0–0.15) samples. (b) Comparison of zoomed powder XRD patterns of $Sn_{1-x}Sb_xTe$ with a Sn-based layered intergrowth compound. (c) Lattice parameter (a) *vs.* Sb concentration (x) in $Sn_{1-x}Sb_xTe$ (x = 0–0.2).

$\sim$8.62 W m^{-1} K^{-1} to $\sim$3.4 W m^{-1} K^{-1} for $Sn_{0.8}Sb_{0.2}Te$ at 300 K, which is $\sim$61% reduction compared to pristine SnTe. This large reduction in κ_{total} is attributed to both the significant reduction of κ_{el} caused by the donor nature of Sb^{3+} in SnTe (Fig. 2b) and the reduction of κ_{lat} (Fig. 2c). Typically, in $Sn_{0.85}Sb_{0.15}Te$, room temperature κ_{total} exhibits a value of $\sim$3.58 W m^{-1} K^{-1} which decreases to $\sim$1.9 W m^{-1} K^{-1} at 825 K.

κ_{lat} was obtained by subtracting the electronic thermal conductivity, κ_{el}, from κ_{total} (Fig. 2c). The electronic contribution of thermal conductivity was extracted based on the fitting of temperature dependent Seebeck coefficients that estimate the reduced chemical potential, from which the Lorenz number, L, has been calculated as explained in previous literature (Fig. S4, ESI†).[27] With the increasing Sb content, room temperature κ_{lat} decreases gradually and reaches the minimum value of $\sim$0.67 W m^{-1} K^{-1} for the $Sn_{0.85}Sb_{0.15}Te$ sample. The Klemens–Drabble (KD) model of disordered alloys was applied to predict the variation of lattice thermal conductivity of the $Sn_{1-x}Sb_xTe$ system (see Fig. S5, ESI†).[28] The required fitting parameters have been adopted from previous literature.[15b] For $Sn_{0.96}Sb_{0.04}Te$, $Sn_{0.92}Sb_{0.08}Te$ and $Sn_{0.88}Sb_{0.12}Te$, experimental κ_{lat} values agree well with the KD model, indicating the point defect scattering caused by Sb alloying as the dominant factor for phonon scattering with low Sb content in SnTe (Fig. S5, ESI†). However, when x is >0.12 in $Sn_{1-x}Sb_xTe$, the experimental κ_{lat} lies far below the KD theory line, indicating that additional phonon scattering mechanisms are operative in addition to point defect scattering. The minimum κ_{lat} values obtained in the present $Sn_{1-x}Sb_xTe$ ingot samples are indeed lower than those previously reported for the $Sn_{1-x}In_xTe$,[18a] Hg/Mn/Cd alloyed SnTe[17a,c,21] and SnTe–$AgBiTe_2$ system[17b] (Fig. 2d). Temperature dependent κ_{lat} of $Sn_{0.85}Sb_{0.15}Te$ is found to be close to the theoretical minimum of the lattice thermal conductivity of SnTe (Fig. 2c), which is calculated by the use of the model proposed by Cahill *et al.*[29]

In order to investigate the underlying mechanisms of the observed low lattice thermal conductivities of $Sn_{1-x}Sb_xTe$, we have performed a detailed nanostructural examination using transmission electron microscopy (TEM) (see Fig. 3). Although the PXRD patterns of $Sn_{1-x}Sb_xTe$, $x < 0.12$ indicate "single phase" nature, TEM images of $Sn_{1-x}Sb_xTe$ revealed the presence of numerous nanoscale precipitates thought to be favorable for phonon scattering. The TEM images of all ingots showed similar features, and therefore we only show images from the samples of the composition $Sn_{0.96}Sb_{0.04}Te$, $Sn_{0.92}Sb_{0.08}Te$ and $Sn_{0.85}Sb_{0.15}Te$. In Fig. 3a, Fig. S6a and b, ESI,† we show typical low magnification TEM images of $Sn_{0.96}Sb_{0.04}Te$, $Sn_{0.92}Sb_{0.08}Te$ and

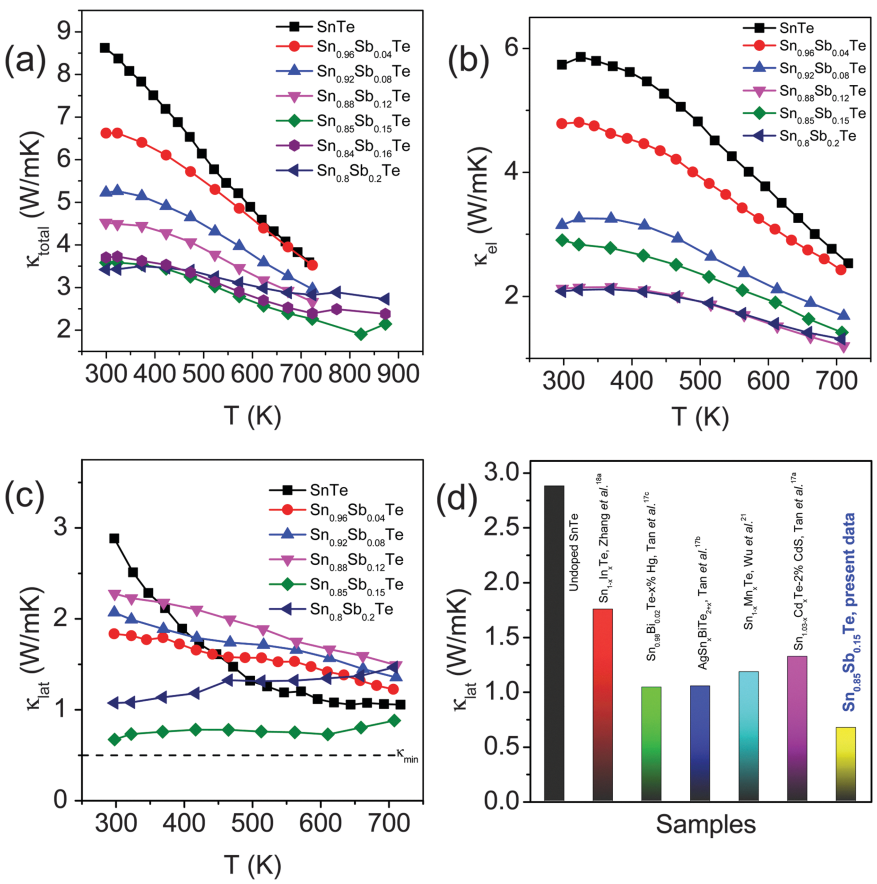

Fig. 2 Temperature-dependent (a) total thermal conductivity (κ_{total}), (b) electronic thermal conductivity (κ_{el}) and (c) lattice thermal conductivity (κ_{lat}) of $Sn_{1-x}Sb_xTe$ samples. (d) Comparison of the room temperature κ_{lat} of the present $Sn_{0.85}Sb_{0.15}Te$ sample with that of the previously reported high performance $Sn_{1-x}In_xTe$,[18a] Hg/Mn/Cd[17a,c,21] alloyed SnTe and SnTe–$AgBiTe_2$.[17b]

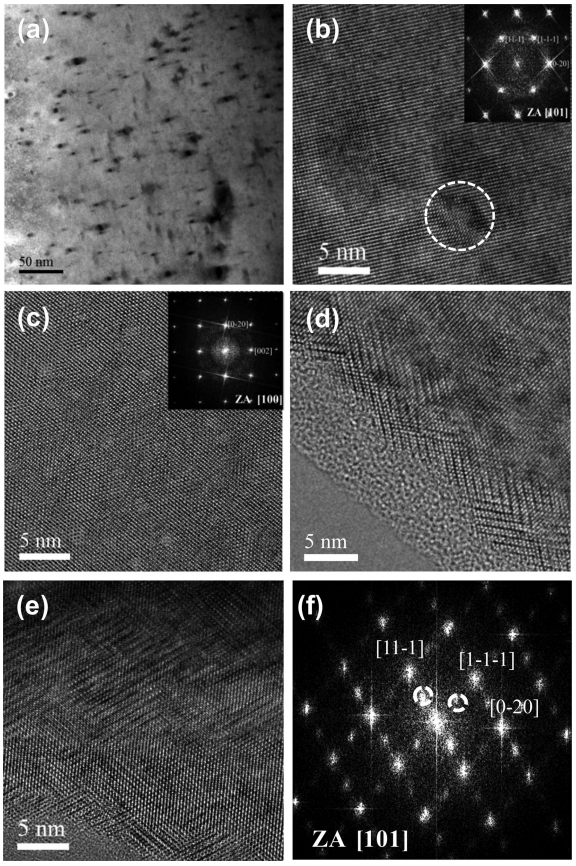

Fig. 3 Transmission electron microscopy of samples $Sn_{0.96}Sb_{0.04}Te$, $Sn_{0.92}Sb_{0.08}Te$ and $Sn_{0.85}Sb_{0.15}Te$. (a) Low-magnification TEM image of sample $Sn_{0.96}Sb_{0.04}Te$ showing nanoscale precipitates. (b) HRTEM image of one of the precipitates of the $Sn_{0.96}Sb_{0.04}Te$ sample, showing coherent interfaces, highlighted by the circle. The corresponding inset FFT pattern indexed to the cubic rocksalt structure. (c) HRTEM image of $Sn_{0.92}Sb_{0.08}Te$ showing the presence of criss-cross lines with the angle of 60° between them. The corresponding inset FFT pattern indexed to the cubic rocksalt structure. Panels (d) and (e) are HRTEM images of $Sn_{0.85}Sb_{0.15}Te$ showing the nanodomains of layered intergrowth nanostructures. (f) FFT pattern indexed to the cubic rocksalt structure with white circles indicating superstructure ordering spots at 1/2 (*h*, *k*, *l*) with *h*, *k*, *l* value of (1, 1, 1).

$Sn_{0.85}Sb_{0.15}Te$ samples, respectively. All images confirm the presence of various nanoscale precipitates (2–10 nm) with a dark contrast. The endotaxial nature of the nanoprecipitates was confirmed from the electron diffraction pattern, shown in the inset of Fig. 3b and c, which can be indexed based only on the cubic rocksalt SnTe structure. The size of these small endotaxial nanoprecipitates is similar to that of the mean free path of the heat carrying phonon in SnTe,[9] thus they effectively scatter phonons and reduce κ_{lat} in SnTe. Though it is difficult to quantitatively determine the exact compositions of individual precipitates owing to their overlap with the matrix, energy dispersive X-ray spectroscopy (EDAX) indicates an increase in the Sb signal from the precipitates compared with the matrix regions (Fig. S7, ESI†).

For further analysis, we have performed high-resolution TEM (HRTEM) investigations on $Sn_{1-x}Sb_xTe$ samples. Fig. 3b and Fig. S6c, ESI† show typical phase contrast HRTEM images containing several nanoprecipitates for $Sn_{0.96}Sb_{0.04}Te$. High-resolution imaging shows that the nanoinclusions are coherent with the matrix. Such a coherent interface can contribute to the scattering of phonon with medium and long wavelengths, meanwhile maintaining good carrier transport without excessive scattering.[4] Therefore, under appropriate carrier doping one can expect relatively high mobility. Hence, these nanoscale features are unique in terms of enhancing the performance of thermoelectric properties of SnTe.

The HRTEM image of $Sn_{0.92}Sb_{0.08}Te$ shows the existence of characteristics of layered criss-cross lines oriented along [111] planes with 60° angle between them (see Fig. 3c). Such layered nanostructures (10–30 nm) become prominent in the $Sn_{0.85}Sb_{0.15}Te$ sample (HRTEM images in Fig. 3d and e, and Fig. S6d, ESI†). These HRTEM images indicate the presence of layered superstructure nanodomains with features similar to those exhibited in $Na_{1-x}Pb_mSbyTe_{m+2}$ samples.[30] A mention must be made of the fact that the superlattice spots along the ⟨111⟩ direction are observed in the fast Fourier transform (FFT) image of the $Sn_{0.85}Sb_{0.15}Te$ sample (Fig. 3f). This indicates a doubling of the lattice period along the ⟨111⟩ directions in real space. At higher Sb concentrations, local Sb segregation along the ⟨111⟩ directions of cubic SnTe forms the nanodomains of layered intergrowth $Sn_mSb_{2n}Te_{3n+m}$, which are embedded in SnTe matrix. Hence, the presence of superlattice spots along the ⟨111⟩ direction and an extra peak in the PXRD pattern of $Sn_{0.85}Sb_{0.15}Te$ indicate the formation of layered intergrowth nanostructures of Sb rich $Sn_mSb_{2n}Te_{3n+m}$ compounds. These compounds are known to show superstructure ordering spots in electron diffraction due to the modulated intergrowth structure and large unit cell.[31] Superlattice structures generally affect the lattice thermal conductivity *via* various ways, including modification of the phonon spectrum and phonon localization, and diffuse or specular scattering of phonons at interfaces due to acoustic mismatch.[32] Here, the presence of nanodomains of Sb rich layered $Sn_mSb_{2n}Te_{3n+m}$ in SnTe scatters the phonons efficiently through both (a) the interface between matrix (SnTe) and nanodomain and (b) the interfaces between the heterostructured layers within $Sn_mSb_{2n}Te_{3n+m}$. The melting points of most of the layered intergrowth compounds in the homologous series, $M_m(Sb/Bi)_{2n}Te_{3n+m}$, where M: Ge/Sn/Pb, are incongruent; thus, the synthesis of pure bulk phases through traditional high-temperature solid-state melting techniques is really challenging.[26a,b,33] Here, we show the stabilization of these layered intergrowth phases in the form of nanodomains through matrix encapsulation, which is intriguing in terms of fundamental solid state inorganic chemistry. Earlier, kinetic low temperature syntheses have been demonstrated the stabilization of the pure-phase compounds in the $Pb_mBi_{2n}Te_{3n+m}$ family in the form of layered nanosheets.[26b]

Fig. 4 shows the temperature dependent electrical transport properties of $Sn_{1-x}Sb_xTe$ samples. The room temperature Hall coefficients, R_H, of all $Sn_{1-x}Sb_xTe$ (x = 0–0.20) samples are positive, which indicate the p-type conduction in this system. For all samples, the electrical conductivity (σ) decreases with the increase in temperature, which is typically observed for a degenerate semiconductor (Fig. 4a). At room temperature, σ decreases gradually with the increase in donor Sb content in

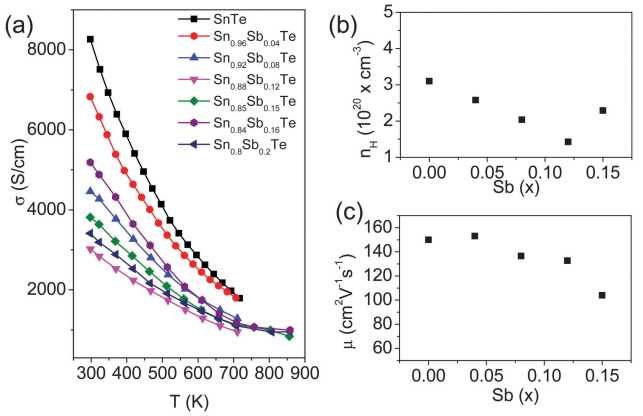

Fig. 4 (a) Temperature dependent electrical conductivity (σ) of $Sn_{1-x}Sb_xTe$ samples. (b) Carrier concentration (n) and (c) carrier mobility (μ) at room temperature with respect to Sb concentration (x) in $Sn_{1-x}Sb_xTe$.

SnTe due to the systematic reduction in p-type carrier concentration, n (Fig. 4b). The reduction of hole concentration is attributed to the substitution of aliovalent Sb^{3+} at the Sn^{2+} site in SnTe that contributes the excess electrons to the system from the chemical valence count. Near room temperature, pristine SnTe exhibits a σ value of $\sim$8265 S cm^{-1}, which drastically reduces to $\sim$3032 S cm^{-1} for the composition of $Sn_{0.88}Sb_{0.12}Te$. Further increase in Sb concentration above x = 0.12 leads to an increase in the σ value from $\sim$3032 to $\sim$3816 S cm^{-1} for the $Sn_{0.85}Sb_{0.15}Te$ sample. The increase in the σ value of Sb concentration above 12 mol% in SnTe is attributed to the increase in hole concentration (Fig. 4b), which results due to the phase separation of Sb-rich $Sn_mSb_{2n}Te_{3n+m}$ nanodomains. This phase segregation is correlated with the formation of nanostructures, which actually alters the chemical composition of the matrix, and thereby the hole density.[17b] A mention must be made that the carrier mobility (μ) remains nearly same (Fig. 4c) in the case of lower Sb content in SnTe due to endotaxial nature of the nanoprecipitates, which is indeed beneficial for electronic transport.

Fig. 5a represents the temperature dependence of Seebeck coefficient (S) of $Sn_{1-x}Sb_xTe$ samples. A positive value of S indicates the p-type conduction in the measured temperature range of 300–860 K, which agrees with the Hall measurement. Pristine SnTe exhibits an S value of $\sim$20 μV K^{-1} at 300 K and reaches the maximum value of $\sim$90 μV K^{-1} at 700 K. The substitution of Sb in SnTe significantly increases the S value from $\sim$20 μV K^{-1} to $\sim$40 μV K^{-1} at 300 K. Typically, the room temperature S value of $Sn_{0.85}Sb_{0.15}Te$ is $\sim$34 μV K^{-1}, which increases with temperature and reaches the maximum value of $\sim$158 μV K^{-1} at 856 K. Above 800 K, S starts decreasing with further increase in temperature for $Sn_{1-x}Sb_xTe$, $x > 0.15$, which corresponds to the onset of bipolar conduction.

A room temperature Pisarenko plot, Seebeck coefficient (S) as a function of carrier density (n), of $Sn_{1-x}Sb_xTe$ is shown in Fig. 5b. Theoretical Pisarenko curves have been calculated by considering the contribution of both the light hole (L point) and heavy hole valence band (Σ point) of un-doped SnTe.[18a]

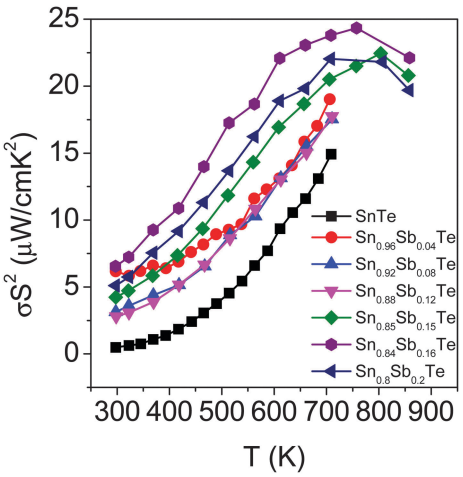

Fig. 6 Temperature dependence of power factor (σS^2) of $Sn_{1-x}Sb_xTe$ samples.

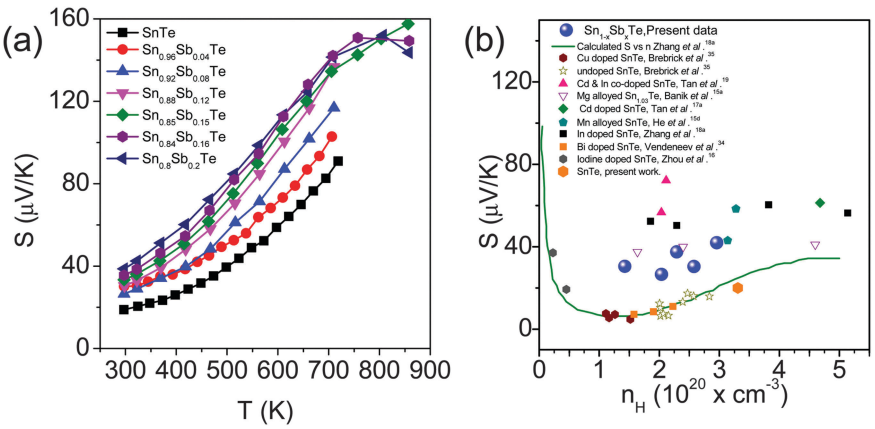

Fig. 5 (a) Temperature dependent Seebeck coefficient (S) of $Sn_{1-x}Sb_xTe$ samples; (b) room temperature S *vs.* n plot of the present $Sn_{1-x}Sb_xTe$ samples. For comparison, previously reported S *vs.* n experimental data of un-doped SnTe,[35] Cu-doped SnTe,[35] Cd and In doped SnTe,[19] Mg alloyed SnTe,[15a] Cd doped SnTe,[17a] Mn doped SnTe,[15d] In doped SnTe,[18a] Bi doped SnTe,[34] iodine doped SnTe[16] and theoretical a Pisarenko curve based on the VBM model[18a] are given in (b).

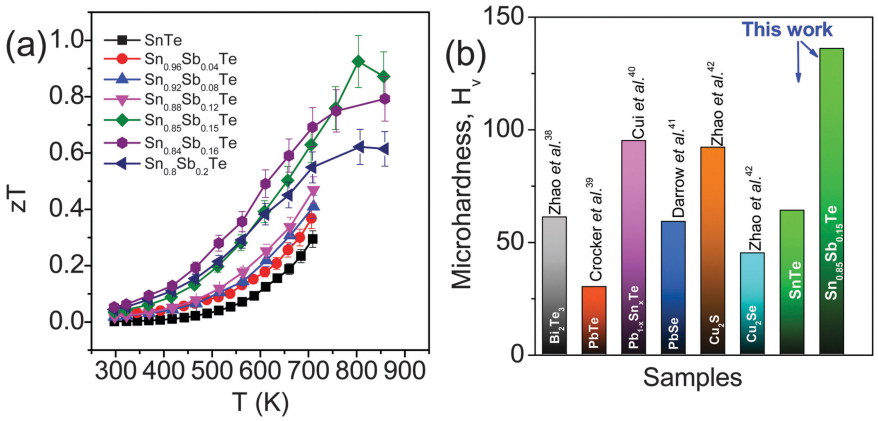

Fig. 7 (a) Temperature dependence of thermoelectric figure of merit (zT) of $Sn_{1-x}Sb_xTe$ samples with 10% error bar. (b) Vickers microhardness value (H_V) of $Sn_{1-x}Sb_xTe$ (x = 0, 0.15) samples compared with other thermoelectric materials.

Here, we have compared the present S *vs.* n data of the present $Sn_{1-x}Sb_xTe$ with the previously reported data of In doped SnTe,[18a] Mg doped SnTe,[15a] Cd doped SnTe,[17a] Bi doped SnTe,[34] Cu doped SnTe,[35] Mn alloyed SnTe,[15d] iodine doped SnTe,[16] and Cd and In co-doped SnTe[19], and also with the earlier reported theoretical S *vs.* n curve by Zhang *et al.*[18a] Particularly, S values of $Sn_{1-x}In_xTe$ and Cd/Mg/Hg/Mn alloyed SnTe samples lie far above the theoretical Pisarenko line due to the effect of resonant level formation and valence band convergence, respectively. Here, room temperature S values of $Sn_{1-x}Sb_xTe$ samples also reside slightly above the Pisarenko curve. The widely dispersed nanostructures in SnTe are responsible for this unusual behavior. This originates probably due to energy dependent scattering of carriers, leading to an energy filtering effect that enhances the Seebeck coefficient.[36] A similar trend was earlier observed for $AgSbTe_2$–SnTe based alloys.[37]

Fig. 6 presents temperature dependence of the power factor (σS^2) of $Sn_{1-x}Sb_xTe$ (x = 0.00–0.20) samples. Benefiting from optimized electrical conductivity and enhancement in Seebeck coefficients, the $Sn_{1-x}Sb_xTe$ samples exhibit significantly higher power factors than those of pristine SnTe samples, with maximum values touching $\sim$25 μW cm^{-1} K^{-2} for $Sn_{0.84}Sb_{0.16}Te$ at 750 K.

In Fig. 7a, we have presented temperature dependent thermoelectric figure of merits, zT, of $Sn_{1-x}Sb_xTe$ (x = 0–0.2). The samples show a systematic increase of zT with the increasing Sb content in SnTe at around room temperature; however, the occurrence of bipolar conduction seen in the samples with high Sb content ($x \geq 0.15$) leads to the deterioration of zT at high temperatures. The highest zT value of $\sim$1 was achieved for $Sn_{0.85}Sb_{0.15}Te$ at 800 K, which is significantly higher compared to the undoped SnTe sample.

Besides the promising zT, one has to look for the good mechanical properties of thermoelectric materials for mass-market applications. The micro-hardness values of SnTe and $Sn_{0.85}Sb_{0.15}Te$ samples were measured on the Vickers scale using the micro-hardness indentation method (Fig. 7b). Undoped SnTe has a hardness value of $\sim$65 H_V. The substitution of Sb in SnTe increases the micro-hardness value to $\sim$136 H_V ($\sim$109% increment in H_V value) for the composition of $Sn_{0.85}Sb_{0.15}Te$. The increase in Vickers micro-hardness (H_V) in $Sn_{1-x}Sb_xTe$ is mainly due to the significant reduction of defects and Sn vacancies caused by Sb substitution. Additionally, nanoscale precipitates block the movement of dislocations in SnTe, which further improves the micro-hardness in $Sn_{1-x}Sb_xTe$. The obtained micro-hardness value of $\sim$136 H_V for $Sn_{0.85}Sb_{0.15}Te$ is significantly higher than that of the state-of-the-art thermoelectric materials such as Bi_2Te_3,[38] PbTe,[39] $Pb_{1-x}Sn_xTe$,[40] PbSe,[41] Cu_2S,[42] and Cu_2Se.[42]

4. Conclusions

In conclusion, $Sn_{1-x}Sb_xTe$ exhibits an ultralow lattice thermal conductivity approaching the theoretical minimum limit, which is attributed to the formation of spontaneous nano-domains of Sb rich layered intergrowth $Sn_mSb_{2n}Te_{3n+m}$ in SnTe through matrix encapsulation. The segregation of Sb along the ⟨111⟩ direction of SnTe leads to the formation of superlattice structure which resulted in significant phonon scattering to effectively lower κ_{lat}. Additionally, Sb doping in SnTe decreases p-type carrier density due to aliovalent donor dopant nature of Sb^{3+} at the Sn^{2+} site in SnTe. A significant enhancement in the Seebeck coefficient has been achieved due to simultaneous reduction of carrier density and carrier filtering through super-structure nanodomain formation. Hence, the enhanced thermoelectric figure of merit, zT, of $\sim$1 at 800 K has been obtained for the composition of $Sn_{0.85}Sb_{0.15}Te$. For the high zT sample, the measured Vickers microhardness value was $\sim$136 H_V, which is about $\sim$109% higher compared to that of pristine SnTe ($\sim$65 H_V).

Acknowledgements

We thank Prof. C. N. R. Rao for enormous support and the TEM facility in ICMS, JNCASR. This work was partially supported by the Department of Science & Technology (DST), the Department of Atomic Energy (DAE) BRNS-YSRA and Sheikh Saqr Laboratory projects. A. B. thanks the INSPIRE Programme for PhD fellowship.

We thank Mr Somnath Ghara for his help during Hall measurements. We thank Prof. A. M. Umarji, IISc, for providing access to the microhardness measurement facility.

References

1 (*a*) L.-D. Zhao, V. P. Dravid and M. G. Kanatzidis, *Energy Environ. Sci.*, 2014, **7**, 251–268; (*b*) J. R. Sootsman, D. Y. Chung and M. G. Kanatzidis, *Angew. Chem., Int. Ed.*, 2009, **48**, 8616–8639; (*c*) G. J. Snyder and E. S. Toberer, *Nat. Mater.*, 2008, **7**, 105–114; (*d*) B. Poudel, Q. Hao, Y. Ma, Y. Lan, A. Minnich, B. Yu, X. Yan, D. Wang, A. Muto, D. Vashaee, X. Chen, J. Liu, M. S. Dresselhaus, G. Chen and Z. Ren, *Science*, 2008, **320**, 634–638; (*e*) X. Zhang and L.-D. Zhao, *J. Materiomics*, 2015, **1**, 92–105.

2 S. I. Kim, K. H. Lee, H. A. Mun, H. S. Kim, S. W. Hwang, J. W. Roh, D. J. Yang, W. H. Shin, X. S. Li, Y. H. Lee, G. J. Snyder and S. W. Kim, *Science*, 2015, **348**, 109–114.

3 K. Biswas, J. He, I. D. Blum, C.-I. Wu, T. P. Hogan, D. N. Seidman, V. P. Dravid and M. G. Kanatzidis, *Nature*, 2012, **489**, 414–418.

4 K. Biswas, J. He, Q. Zhang, G. Wang, C. Uher, V. P. Dravid and M. G. Kanatzidis, *Nat. Chem.*, 2011, **3**, 160–166.

5 W. Qiu, L. Xi, P. Wei, X. Ke, J. Yang and W. Zhang, *Proc. Natl. Acad. Sci. U. S. A.*, 2014, **111**, 15031–15035.

6 (*a*) H. Euchner, S. Pailhès, L. T. K. Nguyen, W. Assmus, F. Ritter, A. Haghighirad, Y. Grin, S. Paschen and M. de Boissieu, *Phys. Rev. B: Condens. Matter Mater. Phys.*, 2012, **86**, 224303; (*b*) X. Shi, J. Yang, J. R. Salvador, M. Chi, J. Y. Cho, H. Wang, S. Bai, J. Yang, W. Zhang and L. Chen, *J. Am. Chem. Soc.*, 2011, **133**, 7837–7846; (*c*) M. K. Jana, K. Pal, U. V. Waghmare and K. Biswas, *Angew. Chem., Int. Ed.*, 2016, DOI: 10.1002/anie.201511737.

7 L. Bjerg, B. B. Iversen and G. K. H. Madsen, *Phys. Rev. B: Condens. Matter Mater. Phys.*, 2014, **89**, 024304.

8 (*a*) S. N. Guin, J. Pan, A. Bhowmik, D. Sanyal, U. V. Waghmare and K. Biswas, *J. Am. Chem. Soc.*, 2014, **136**, 12712–12720; (*b*) H. Liu, X. Shi, F. Xu, L. Zhang, W. Zhang, L. Chen, Q. Li, C. Uher, T. Day and G. J. Snyder, *Nat. Mater.*, 2012, **11**, 422–425.

9 S. Lee, K. Esfarjani, T. Luo, J. Zhou, Z. Tian and G. Chen, *Nat. Commun.*, 2014, **5**, DOI: 10.1038/ncomms4525.

10 (*a*) S. N. Guin, A. Chatterjee, D. S. Negi, R. Datta and K. Biswas, *Energy Environ. Sci.*, 2013, **6**, 2603–2608; (*b*) D. Morelli, V. Jovovic and J. Heremans, *Phys. Rev. Lett.*, 2008, **101**, 035901.

11 (*a*) L.-D. Zhao, S.-H. Lo, Y. Zhang, H. Sun, G. Tan, C. Uher, C. Wolverton, V. P. Dravid and M. G. Kanatzidis, *Nature*, 2014, **508**, 373–377; (*b*) L.-D. Zhao, G. Tan, S. Hao, J. He, Y. Pei, H. Chi, H. Wang, S. Gong, H. Xu, V. P. Dravid, C. Uher, G. J. Snyder, C. Wolverton and M. G. Kanatzidis, *Science*, 2016, **351**, 141–144.

12 (*a*) Y. Pei, X. Shi, A. LaLonde, H. Wang, L. Chen and G. J. Snyder, *Nature*, 2011, **473**, 66–69; (*b*) K. Biswas, J. He, G. Wang, S.-H. Lo, C. Uher, V. P. Dravid and M. G. Kanatzidis, *Energy Environ. Sci.*, 2011, **4**, 4675–4684; (*c*) S. N. Girard, J. He, X. Zhou, D. Shoemaker, C. M. Jaworski, C. Uher, V. P. Dravid, J. P. Heremans and M. G. Kanatzidis, *J. Am. Chem. Soc.*, 2011, **133**, 16588–16597; (*d*) J. P. Heremans, V. Jovovic, E. S. Toberer, A. Saramat, K. Kurosaki, A. Charoenphakdee, S. Yamanaka and G. J. Snyder, *Science*, 2008, **321**, 554–557.

13 (*a*) L. M. Rogers, *J. Phys. D: Appl. Phys.*, 1968, **1**, 845; (*b*) B. Efimova, V. Kaidanov, B. Y. Moizhes and I. Chernik, *Sov. Phys. Solid State*, 1966, **7**, 2032–2034.

14 R. Brebrick, *J. Phys. Chem. Solids*, 1963, **24**, 27–36.

15 (*a*) A. Banik, U. S. Shenoy, S. Anand, U. V. Waghmare and K. Biswas, *Chem. Mater.*, 2015, **27**, 581–587; (*b*) G. Tan, F. Shi, S. Hao, H. Chi, T. P. Bailey, L.-D. Zhao, C. Uher, C. Wolverton, V. P. Dravid and M. G. Kanatzidis, *J. Am. Chem. Soc.*, 2015, **137**, 11507–11516; (*c*) R. Al Rahal Al Orabi, N. A. Mecholsky, J. Hwang, W. Kim, J.-S. Rhyee, D. Wee and M. Fornari, *Chem. Mater.*, 2016, **28**, 376–384; (*d*) J. He, X. Tan, J. Xu, G. Liu, H. Shao, Y. Fu, X. Wang, Z. Liu, J. Xu, H. Jiang and J. Jiang, *J. Mater. Chem. A*, 2015, **3**, 19974–19979; (*e*) A. Banik and K. Biswas, *J. Solid State Chem.*, DOI: 10.1016/j.jssc.2016.02.012.

16 M. Zhou, Z. M. Gibbs, H. Wang, Y. Han, C. Xin, L. Li and G. J. Snyder, *Phys. Chem. Chem. Phys.*, 2014, **16**, 20741–20748.

17 (*a*) G. Tan, L.-D. Zhao, F. Shi, J. W. Doak, S.-H. Lo, H. Sun, C. Wolverton, V. P. Dravid, C. Uher and M. G. Kanatzidis, *J. Am. Chem. Soc.*, 2014, **136**, 7006–7017; (*b*) G. Tan, F. Shi, H. Sun, L.-D. Zhao, C. Uher, V. P. Dravid and M. G. Kanatzidis, *J. Mater. Chem. A*, 2014, **2**, 20849–20854; (*c*) G. Tan, F. Shi, J. W. Doak, H. Sun, L.-D. Zhao, P. Wang, C. Uher, C. Wolverton, V. P. Dravid and M. G. Kanatzidis, *Energy Environ. Sci.*, 2015, **8**, 267–277; (*d*) L.-D. Zhao, X. Zhang, H. Wu, G. Tan, Y. Pei, Y. Xiao, C. Chang, D. Wu, H. Chi, L. Zheng, S. Gong, C. Uher, J. He and M. G. Kanatzidis, *J. Am. Chem. Soc.*, 2016, **138**, 2366–2373.

18 (*a*) Q. Zhang, B. Liao, Y. Lan, K. Lukas, W. Liu, K. Esfarjani, C. Opeil, D. Broido, G. Chen and Z. Ren, *Proc. Natl. Acad. Sci. U. S. A.*, 2013, **110**, 13261–13266; (*b*) A. Banik and K. Biswas, *J. Mater. Chem. A*, 2014, **2**, 9620–9625; (*c*) G. Tan, W. G. Zeier, F. Shi, P. Wang, G. J. Snyder, V. P. Dravid and M. G. Kanatzidis, *Chem. Mater.*, 2015, **27**, 7801–7811.

19 G. Tan, F. Shi, S. Hao, H. Chi, L.-D. Zhao, C. Uher, C. Wolverton, V. P. Dravid and M. G. Kanatzidis, *J. Am. Chem. Soc.*, 2015, **137**, 5100–5112.

20 O. Falkenbach, A. Schmitz, T. Dankwort, G. Koch, L. Kienle, E. Mueller and S. Schlecht, *Chem. Mater.*, 2015, **27**, 7296–7305.

21 H. Wu, C. Chang, D. Feng, Y. Xiao, X. Zhang, Y. Pei, L. Zheng, D. Wu, S. Gong, Y. Chen, J. He, M. G. Kanatzidis and L.-D. Zhao, *Energy Environ. Sci.*, 2015, **8**, 3298–3312.

22 J. R. Sootsman, R. J. Pcionek, H. Kong, C. Uher and M. G. Kanatzidis, *Chem. Mater.*, 2006, **18**, 4993–4995.

23 P. F. P. Poudeu, J. D'Angelo, H. Kong, A. Downey, J. L. Short, R. Pcionek, T. P. Hogan, C. Uher and M. G. Kanatzidis, *J. Am. Chem. Soc.*, 2006, **128**, 14347–14355.

24 K. F. Hsu, S. Loo, F. Guo, W. Chen, J. S. Dyck, C. Uher, T. Hogan, E. K. Polychroniadis and M. G. Kanatzidis, *Science*, 2004, **303**, 818–821.

25 (*a*) J. R. Sootsman, H. Kong, C. Uher, J. J. D'Angelo, C. I. Wu, T. P. Hogan, T. Caillat and M. G. Kanatzidis, *Angew. Chem.*,

2008, **120**, 8746–8750; (*b*) K. Hoang, S. D. Mahanti and M. G. Kanatzidis, *Phys. Rev. B: Condens. Matter Mater. Phys.*, 2010, **81**, 115106.

26 (*a*) L. E. Shelimova, O. G. Karpinskii, P. P. Konstantinov, E. S. Avilov, M. A. Kretova and V. S. Zemskov, *Inorg. Mater.*, 2004, **40**, 451–460; (*b*) A. Chatterjee and K. Biswas, *Angew. Chem., Int. Ed.*, 2015, **54**, 5623–5627; (*c*) B. A. Kuropatwa and H. Kleinke, *Z. Anorg. Allg. Chem.*, 2012, **638**, 2640–2647.

27 L.-D. Zhao, S.-H. Lo, J. He, H. Li, K. Biswas, J. Androulakis, C.-I. Wu, T. P. Hogan, D.-Y. Chung, V. P. Dravid and M. G. Kanatzidis, *J. Am. Chem. Soc.*, 2011, **133**, 20476–20487.

28 P. G. Klemens, *Phys. Rev.*, 1960, **119**, 507–509.

29 D. G. Cahill, S. K. Watson and R. O. Pohl, *Phys. Rev. B: Condens. Matter Mater. Phys.*, 1992, **46**, 6131–6140.

30 P. F. P. Poudeu, J. D'Angelo, A. D. Downey, J. L. Short, T. P. Hogan and M. G. Kanatzidis, *Angew. Chem., Int. Ed.*, 2006, **118**, 3919–3923.

31 S. Kuypers, G. van Tendeloo, J. van Landuyt and S. Amelinckx, *J. Solid State Chem.*, 1988, **76**, 102–108.

32 (*a*) P. Hyldgaard and G. D. Mahan, *Phys. Rev. B: Condens. Matter Mater. Phys.*, 1997, **56**, 10754–10757; (*b*) G. Chen, *Phys. Rev. B: Condens. Matter Mater. Phys.*, 1998, **57**, 14958–14973.

33 Z. S. Aliev, G. I. Ibadova, J.-C. Tedenac and M. B. Babanly, *J. Alloys Compd.*, 2014, **602**, 248–254.

34 V. P. Vedeneev, S. P. Krivoruchko and E. P. Sabo, *Semiconductors*, 1998, **32**, 241–244.

35 R. Brebrick and A. Strauss, *Phys. Rev.*, 1963, **131**, 104.

36 S. V. Faleev and F. Léonard, *Phys. Rev. B: Condens. Matter Mater. Phys.*, 2008, **77**, 214304.

37 Z.-B. Xing, Z.-Y. Li, Q. Tan, T.-R. Wei, C.-F. Wu and J.-F. Li, *J. Alloys Compd.*, 2014, **615**, 451–455.

38 L.-D. Zhao, B.-P. Zhang, J.-F. Li, M. Zhou, W.-S. Liu and J. Liu, *J. Alloys Compd.*, 2008, **455**, 259–264.

39 A. Crocker and M. Wilson, *J. Mater. Sci.*, 1978, **13**, 833–842.

40 J. Cui, X. Qian and X. Zhao, *J. Alloys Compd.*, 2003, **358**, 228–234.

41 M. Darrow, W. White and R. Roy, *J. Mater. Sci.*, 1969, **4**, 313–319.

42 L. Zhao, X. Wang, F. Y. Fei, J. Wang, Z. Cheng, S. Dou, J. Wang and G. J. Snyder, *J. Mater. Chem. A*, 2015, **3**, 9432–9437.